Earth, Planets and Space

FULL PAPER Open Access

# Simultaneous observations of equatorial plasma bubbles with an all-sky airglow imager and a HF Doppler sounding system in Taiwan

Hiromi Sejima[1], Keisuke Hosokawa[1*], Hiroyuki Nakata[2], Jaroslav Chum[3], Chien-Hung Lin[4] and Jia-Ting Lin[4]

**Abstract**

High-Frequency Doppler (HFD) sounders at low-latitudes often detect characteristic oblique spreading Doppler traces in the spectrogram, known as Oblique Spread Structure (OSS). OSS has been expected to be generated by the dispersion of radio wave reflection due to equatorial plasma bubbles (EPBs). However, it has not yet been confirmed whether OSS is surely a manifestation of EPB by conducting simultaneous observations of EPB and OSS with different observational techniques. Additionally, it remains unclear what kinds of properties of EPB are reflected in the fine structure of OSS. In this study, we investigated three cases of OSSs and EPBs simultaneously observed by a HFD sounding system and an all-sky airglow imager in Taiwan. For the three cases presented here, the timing of OSS occurrence in the HFD data well coincided with that of the EPB appearance in the airglow data. The frequency shift of OSS is quantitatively explained assuming a radio wave reflection at 250–300 km altitudes. These results strongly indicate that OSS is formed by electron density variations at F-region altitudes accompanying EPB; thus, OSS is a manifestation of EPB in the HFD observations. Furthermore, it was suggested that the fine structure of OSS reflected the branching structure of EPB when the multiple branches of EPB reached the intermediate reflection point of the HFD observation. The detection of EPB occurrence and its fine structure using HFD observation enables monitoring of EPB regardless of weather conditions, which will contribute to monitoring the space weather impact of EPBs, for example, on GNSS navigation, in a wide area.

**Keywords** Equatorial plasma bubbles, Radio propagation, Airglow observation

*Correspondence:
Keisuke Hosokawa
keisuke.hosokawa@uec.ac.jp
Full list of author information is available at the end of the article

**Graphical Abstract**

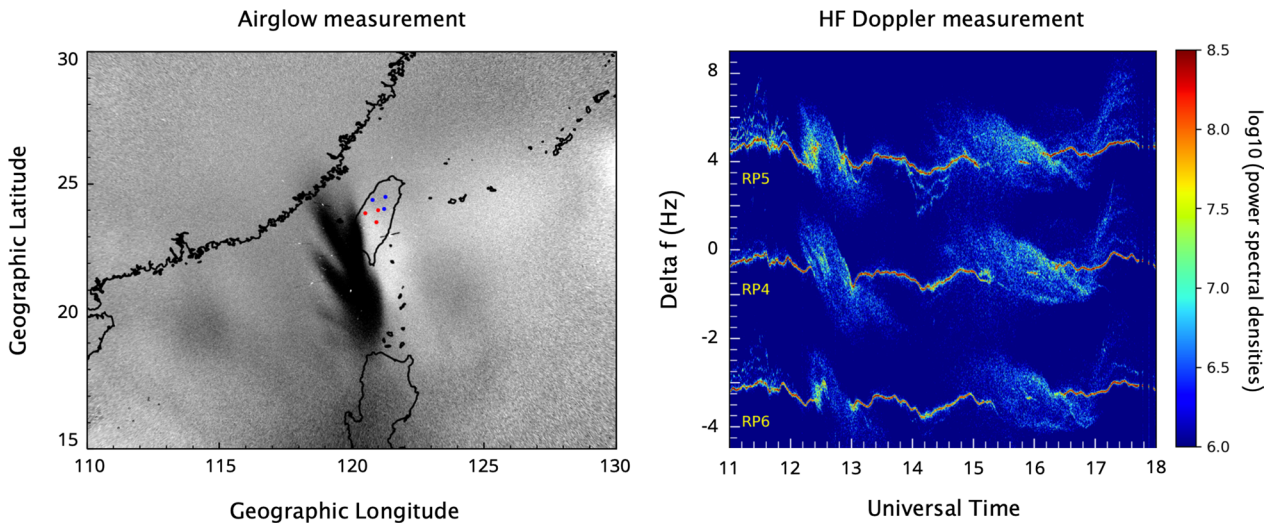


## Introduction

Equatorial Plasma Bubble (EPB) is known as one of the most outstanding disturbances in the F-region ionosphere at equatorial and low-latitude regions. EPBs are recognized as a region where the electron density is reduced compared to the surrounding area (Kil 2015 and references therein). EPBs are generated by the amplification of electron density disturbances that occur in the bottom side of the F region after sunset due to the Rayleigh–Taylor instability, resulting in the growth and uplift of low-density plasma to high altitudes (Woodman and La Hoz, 1976). Because this phenomenon occurs in the whole magnetic flux tubes, the EPBs that grow to higher altitudes can be detected outside the equatorial region, for example, 10–20° away from the magnetic equator.

Electron density perturbations accompanying EPB affect the propagation of radio waves for communication ranging from HF to VHF frequencies (Röttger, 1976; Nakata et al. 2005). Moreover, irregularities in the electron density with different spatial scales are present within EPB, causing diffraction of satellite communication radio waves passing through the ionosphere, leading to the occurrence of so-called ionospheric scintillation when receiving signals from satellites on the ground (Otsuka et al. 2006). Thus, the occurrence of EPBs has a potential to cause interruptions and degradation (in the accuracy) of global navigation satellite systems (GNSS) (e.g., Kintner et al. 2007).

EPBs have been actively investigated within the framework of space weather forecasting, including the evaluation of their impact on the utilization of GNSS. The EPB occurrence climatology has extensively been investigated using various observations. In the Asian sector including Taiwan, where our observations were made, EPBs occur more frequently during equinoxes than during solstices. Statistical studies have shown a positive correlation between the occurrence frequency of EPBs and solar activity (Gentile et al. 2006; Kil et al. 2009). Still, however, factors controlling the daily variability of EPB occurrence have been poorly understood, and predicting their occurrence remains a challenging task.

There are various methods for observing EPBs from the ground. In addition to airglow measurements with all-sky imagers (Weber et al. 1978; Otsuka et al. 2002), remote sensing using radio waves has also been actively employed. For instance, EPBs are detected as Equatorial Spread F (ESF) phenomena by ionosondes (Berkner and Wells 1934). When EPBs occur, the trace of the F region in the ionogram diffuses in both the altitude and frequency directions, hence named as Spread F. ESF is generated by the spatial non-uniformity of the F-region electron density caused by EPBs, which leads to dispersion in reflection height. High-Frequency (HF) Doppler sounding (HFD sounding) has also been used to detect variations of the Doppler frequency associated with EPBs or ESFs (Chum et al. 2014, 2016). Chum et al. (2016) introduced a frequency spreading feature in the Doppler spectrograms obtained from HFD observations in Tucuman, Argentina, and Taiwan during the 2014 solar maximum, which was termed as Oblique Spread Structure (OSS). Since OSS exhibits dispersion in the frequency direction similar to ESF, Chum et al.

(2014, 2016) suggested that OSS is a manifestation of EPB in the HFD observations. Furthermore, Chum et al. (2014, 2016) estimated the propagation velocity of the corresponding density disturbance using the slope of OSS in the Doppler spectrogram and the time delay of the signatures at multiple points and demonstrated that the estimated speed was consistent with the typical eastward propagation of EPBs. It was also reported that the occurrence frequency of OSS is high during a few hours after the local sunset in spring and autumn months in Taiwan and in local summer in Tucumán, Argentina, which again implied that OSS corresponds to EPB-related electron density disturbances.

However, the analysis by Chum et al. (2014, 2016) did not include simultaneous observations with other techniques such as ground-based airglow imaging, making it still unclear whether the occurrence of OSS is truly related to EPB/ESF. More importantly, although fine-scale sub-structures are often observed within OSS, it remains unclarified which characteristics of EPB are reflected by such sub-structures of OSS. In this study, we investigate the relationship between OSS and EPB through simultaneous observations using the HFD sounding system and an all-sky airglow imager at low latitude in Taiwan. Specifically, we aim to confirm whether OSS corresponds to EPB through the analysis of OSS cases observed in Taiwan on March 13 and 16, 2015, and further to elucidate the origin of the fine-scale structures of OSS in the Doppler spectrograms.

## Method

In this study, we utilized 630.0 nm all-sky airglow images obtained by the Lithosphere Atmosphere Space Coupling imager (LASC imager) at Tainan, Taiwan (Glat: 23.1N, Glon: 120.4E, Mlat: 16.4N), operated by National Cheng Kung University to visualize the spatial structure and dynamical characteristics of EPBs. The LASC imager is equipped with an interference optical filter to capture the 630.0 nm airglow emissions from excited oxygen atoms, allowing for the observation of variations in the 630.0 nm airglow emissions associated with EPBs (Rajesh et al. 2017). Figure 1a illustrates an airglow image obtained by the LASC imager at 12:01 UT (LT = UT + 8 h) on March 13, 2015, which has been mapped onto the geographic coordinates by assuming an emission altitude of 250 km following the procedure described in Kubota et al. (2001). To visualize faint airglow variations associated with EPBs, we created an average image using the data acquired within surrounding 1 h of the observation time, and display the deviation component obtained by subtracting the average image from the current single image. A dark region is seen slightly to the southwest of Taiwan, which is the manifestation of an EPB. One can see multiple branch-like structures extending poleward, which is a distinctive feature of EPBs observed in low-latitude regions away from the magnetic equator. In this example, the structure of the EPB extends up to approximately 25° geographic latitude. The emission intensity of 630.0 nm airglow is considered to be approximately proportional to the density of the dominant ion species, oxygen atoms, in

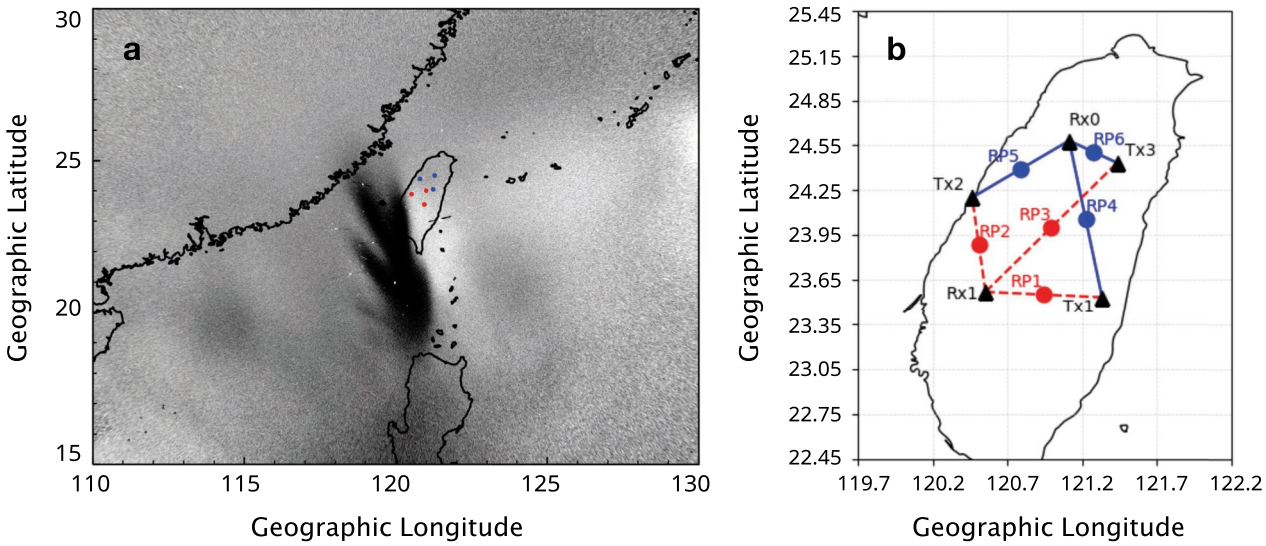


**Fig. 1** **a** A 630.0 nm airglow image captured in Tainan at 12:01 UT on March 13, 2015 at 12:01 UT, mapped onto the geographical coordinates under the assumption of an emission altitude of 250 km. **b** The locations of the transmitting (Tx)/receiving (Rx) stations and the intermediate reflection points of the HFD sounding system in Taiwan. The black triangles represent the Tx and Rx stations, the red circles indicate the intermediate reflection points between the Rx1 and the three Tx stations, and the blue circles represent those between the Rx0 and the three Tx stations

the F-region ionosphere (Sobral et al. 1993). It should be reminded that, however, the emission altitude is slightly lower than the F-region peak due to the dependence of the emission intensity on the altitude distribution of oxygen molecules, that is typically around 250 km.

In addition to airglow data, we employ data obtained by the HFD sounding system, which is operated in Taiwan by the Institute of Atmospheric Physics (IAP) of the Czech Academy of Sciences in collaboration with National Central University, Zhongli, Taiwan. This HFD sounding system is composed of three transmitting stations (Tx1, Tx2, Tx3) and two receiving stations (Rx0, Rx1), as described in Chum et al. (2016) and Lastovicka and Chum (2017). Figure 1b shows the deployment of the HFD sounding system where the intermediate reflection points between the Tx and Rx stations are depicted. The transmitting (Tx) stations emit radio waves with a frequency of 6.57 MHz and a power of 1W, with an offset of ± 4 Hz from the central frequency to identify the source Tx station when signals are captured at the receiving (Rx) stations. The coordinates of the stations deployed in Taiwan are Tx1 (23.897°N, 121.551°E), Tx2 (24.341°N, 120.778°E), Tx3 (24.816°N, 121.727°E), Rx0 (24.972°N, 121.192°E), and Rx1 (23.955°N, 120.927°E). The reflection points between Tx1, Tx2, Tx3, and Rx1 are denoted as RP1, RP2, and RP3, while those between Tx1, Tx2, Tx3, and Rx0 are denoted as RP4, RP5, and RP6. In Fig. 1a, all the six intermediate reflection points are plotted by the red and blue circles, which are well within the field of view of the LASC imager. This enables us to conduct combined simultaneous observations of EPBs using both the optical and radio measurements.

The primary parameter of the HFD sounding is the Doppler frequency shift, which is imposed on radio waves transmitted from the Tx station, reflected in the ionosphere, and received at the Rx station. The Doppler shifts can be used to observe the vertical motion of the ionosphere and the horizontal motion of structures reflecting the radio waves. The Doppler shift, that is usually denoted as $\Delta f$, is given by the following two equations:

$$\Delta f = -\frac{f_0}{c}\frac{dP}{dt}, \tag{1}$$

$$P = \int_S n\, ds, \tag{2}$$

where $f_0$ represents the transmission frequency, $c$ is the speed of light, $P$ is the phase path length, $s$ is the radio propagation path, and $n$ is the refractive index. The sign of the Doppler shift is determined by the differential of the phase path length $P$. Specifically, when the structure reflecting the radio waves approaches the intermediate point of the propagation path horizontally, the phase path length becomes shorter in time, resulting in a positive Doppler shift. Conversely, when the reflection point moves away from the intermediate point, the phase path length becomes longer in time, causing a negative Doppler shift. By monitoring the sign or the temporal variation of the Doppler shift trace that appears in the Doppler spectrogram, it is possible to infer the horizontal motion of the phenomenon causing the reflection. As discussed in Chum et al. (2014, 2016), for the case of the OSS reflection (possible signature of EPB), the Doppler shift in the HFD data is imposed by the change in the phase path length due to the horizontal motion of the reflection point (i.e., EPB); thus, here we do not discuss the vertical motion of the ionosphere during the passage of EPBs. It is worth noting that HFD sounding systems can provide ionospheric reflection data with relatively higher temporal resolution (~ 10 s) than ionograms, thereby enabling the visualization of fine-scale variations/structured embedded within ionospheric phenomena, such as EPB or ESF (Chum et al. 2014).

## Results

We present three EPB cases observed in Taiwan in March 2015. Figure 2a displays the HFD data obtained during the period of 11:00–18:00 UT (19:00–02:00 LT) on March 13, 2015, in the form of a Doppler spectrogram. This spectrogram represents the data obtained from Rx0 including reflections along three observation paths with intermediate reflection points RP4, RP5, and RP6, as shown in Fig. 1b. In each of the three observation paths, clear Doppler frequency peaks were identified as discrete lines of Doppler trace for most of the time, which is considered to correspond to the normal reflection from the F region. However, spreads in the Doppler trace appear during two time periods of 12:15–13:15 UT and 15:00–17:00 UT, where the spreads appear as stripes (we call them "sub-structures") and the frequencies of the sub-structures decrease with time. This is a sign of the occurrence of OSS, which has been suspected to be the manifestation of EPB in the Doppler observation (Chum et al. 2016). For Event 1 observed during the period of 12:15–13:15 UT, it is difficult to recognize any clear internal sub-structures within the OSS although some intensifications of the power spectral density are seen. Event 2 observed during the period of 15:00–17:00 UT lasted longer than did Event 1, but it is also difficult to find sub-structures within the OSS. On the other hand, a distinct spectral density peak similar to normal reflection appeared for a few minutes during Event 2 around 16 UT, indicating a possible internal structure of the OSS. It is noted that data from RP1, RP2, and RP3 are unavailable

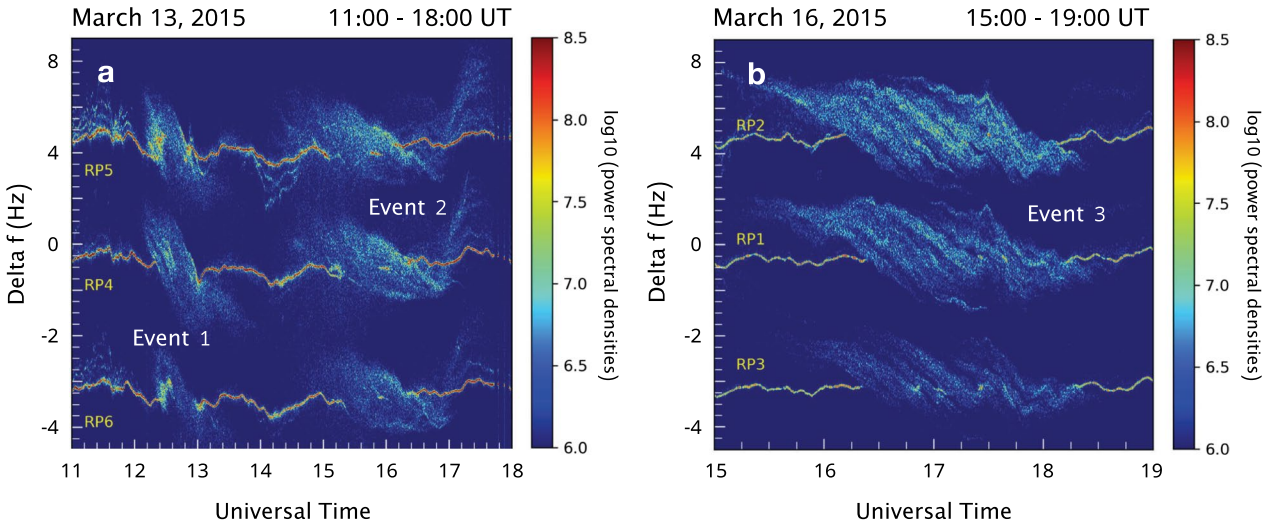


**Fig. 2** Doppler spectrograms obtained by the HFD sounding system in Taiwan in March 2015. **a** Doppler spectrogram obtained from Rx0 for three observation paths, including the intermediate reflection points RP4, RP5, and RP6, during the time interval of 11:00–18:00 UT on March 13, 2015. Two OSS events can be identified during the time intervals of 12:15–13:15 UT (Event 1) and 15:00–17:00 UT (Event 2). **b** Doppler spectrogram obtained during the time interval of 15:00–19:00 UT on March 16, 2015. A large-scale OSS event was identified during the time interval of 16:15–18:15 UT (Event 3)

for Events 1 and 2 and those from RP4, RP5, and RP6 are unavailable for Event 3 because the corresponding Rx system was not operative.

Figure 2b shows a similar case of OSS (Event 3) obtained during the period of 15:00–19:00 UT on March 16, 2015, where data from Rx1 for three observation paths including intermediate reflection points RP1, RP2, and RP3 are displayed. The occurrence of OSS can be confirmed for all the observation paths during the period of 16:15–18:15 UT. Similar to Events 1 and 2, the trace of normal F-region reflection suddenly diffused and the frequency of the diffuse trace decreased in time. However, compared to Events 1 and 2, the duration of this event was longer (observed for almost 2 h), and now we can identify several sub-structures within the OSS, which are seen as oblique structures most clearly in the Doppler trace of RP2.

Figure 3 presents the corresponding 630.0 nm airglow data mapped onto the geographic coordinate system. When mapping the airglow images, we assume that the emission layer of the 630.0 nm airglow is located at an altitude of 250 km. Figure 3a–d displays airglow images obtained during Event 1, which were taken approximately every 10 min. The optical signature of EPB is seen as a dark tree-like structure extending from the bottom of the figure toward the center. As shown in Fig. 3a and b, the EPB branched into three parts at its tip. At least one branch extended to the latitude of the central part of Taiwan, where the intermediate reflection points of the HFD sounding system are located. In particular, as seen in the latest image (Fig. 3d), the tip of this branched structure reached the northernmost part of Taiwan. These four images also reveal that the EPB was moving eastward although the EPB structure is difficult to be confirmed in Fig. 3c due to the presence of clouds.

Figure 3e–h displays airglow images taken during Event 2, with the EPB being identified as multiple dark line structures extending from the bottom of the figure toward the top. Two EPBs reached a latitude of 26.0° beyond the northern tip of Taiwan. These EPBs were also observed to be moving eastward. The timing of the occurrence of these two EPBs on March 13, 2015 coincides well with the interval of OSS occurrence shown in Fig. 2a. Moreover, the fact that the structures of these EPBs swept across the intermediate reflection points of HFD (RP4, 5, 6) strongly suggests that OSS is indeed associated with the appearance of EPBs.

The number of simultaneous observations of OSSs/EPBs in Taiwan was limited even during the previous solar maximum period mainly due to the local weather conditions for airglow measurements and the operational condition of the HFD sounder. However, in addition to the three cases introduced in this paper, we investigated a few additional cases of OSSs/EPBs in February 2014 and obtained similar correspondence between the timings of OSS/EPB appearance, which further confirms that the OSSs are surely the manifestations of EPBs in the HFD sounding measurement.

Figure 3i–l depicts airglow images corresponding to Event 3. The EPB can be recognized again as a dark

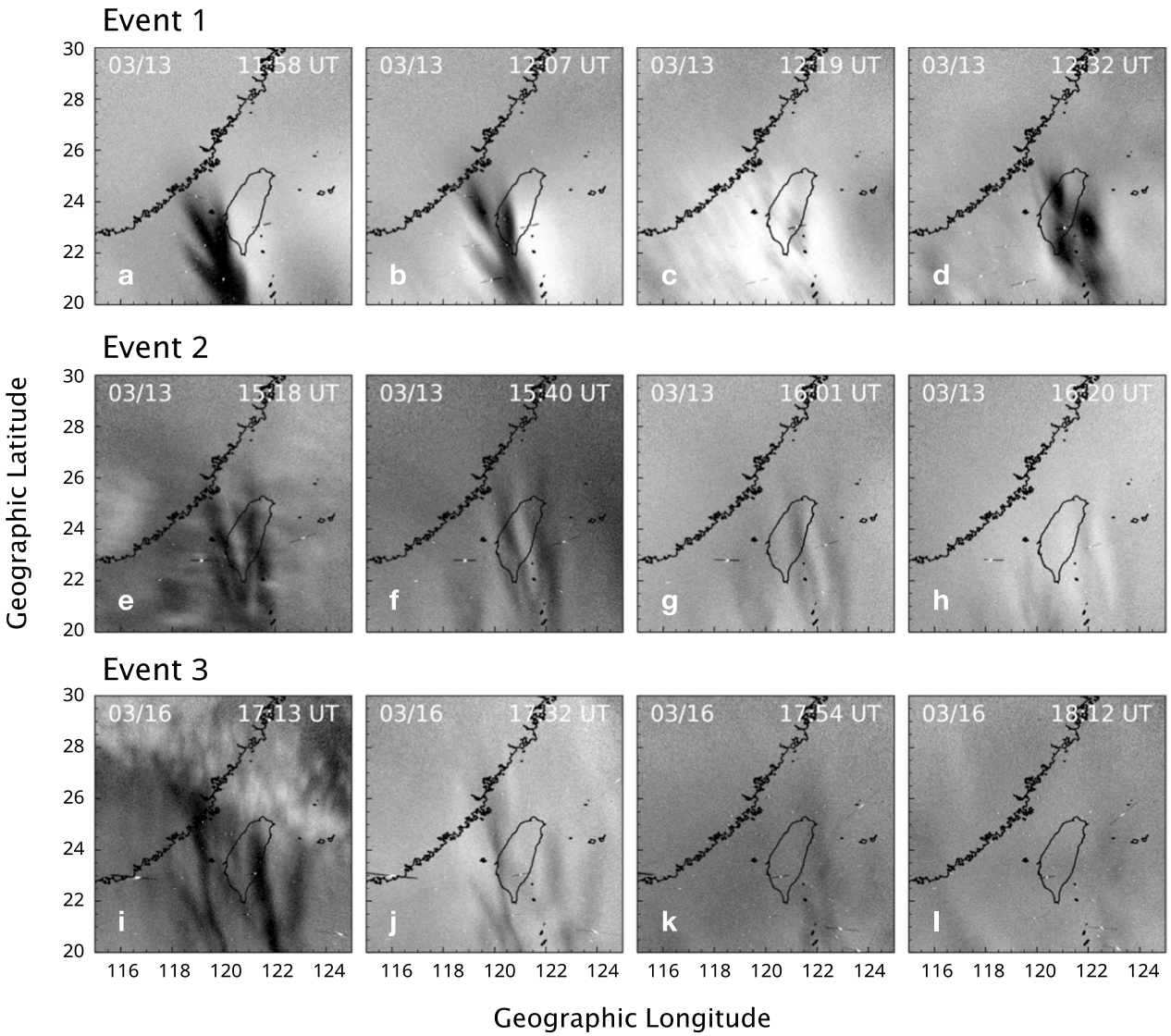


**Fig. 3** 630.0 nm airglow images obtained by the LASC imager in Tainan for three cases of OSS, (**a**–**d**) for Event 1, (**e**–**h**) for Event 2, and (**i**–**l**) for Event 3. The airglow images have been mapped onto the geographic coordinate system by assuming the emission altitude of 250 km

tree-like structure extending upward from the lower part of the figure. Similar to the two cases on March 13, 2015, the EPB branched into multiple arms and exhibited a large spatial structure in the east–west direction. Several branches of the EPB extended to the northernmost part of Taiwan, with the longest one reaching a latitude of 27°. Simultaneous observation of HFD sounder shown in Fig. 2b indicates the existence of multiple Doppler traces (i.e., sub-structures) embedded within the entire OSS structure. The comparison of HFD data with those from the airglow imager implies that the internal structures of OSS manifest the branching feature of EPB, which will be discussed in detail in the Discussion section.

To investigate the propagation characteristics of EPBs in detail, Fig. 4 plots the airglow data during Event 3 as a keogram which is a time series of the optical intensity sampled along the longitudinal direction. Data were extracted along the east–west cross section that includes the geographical latitude of RP1 between Tx1 and Rx1 and plotted as a function of time in the horizontal axis and longitude in the vertical axis. The red dashed line represents the geographic longitude of RP1. During the first half of this time period (15:00–17:00 UT), cloudy sky condition made it difficult to confirm the structure of EPBs. However, after 17:00 UT, the eastward propagation of the EPBs could be observed as black linear structures extending upward to the

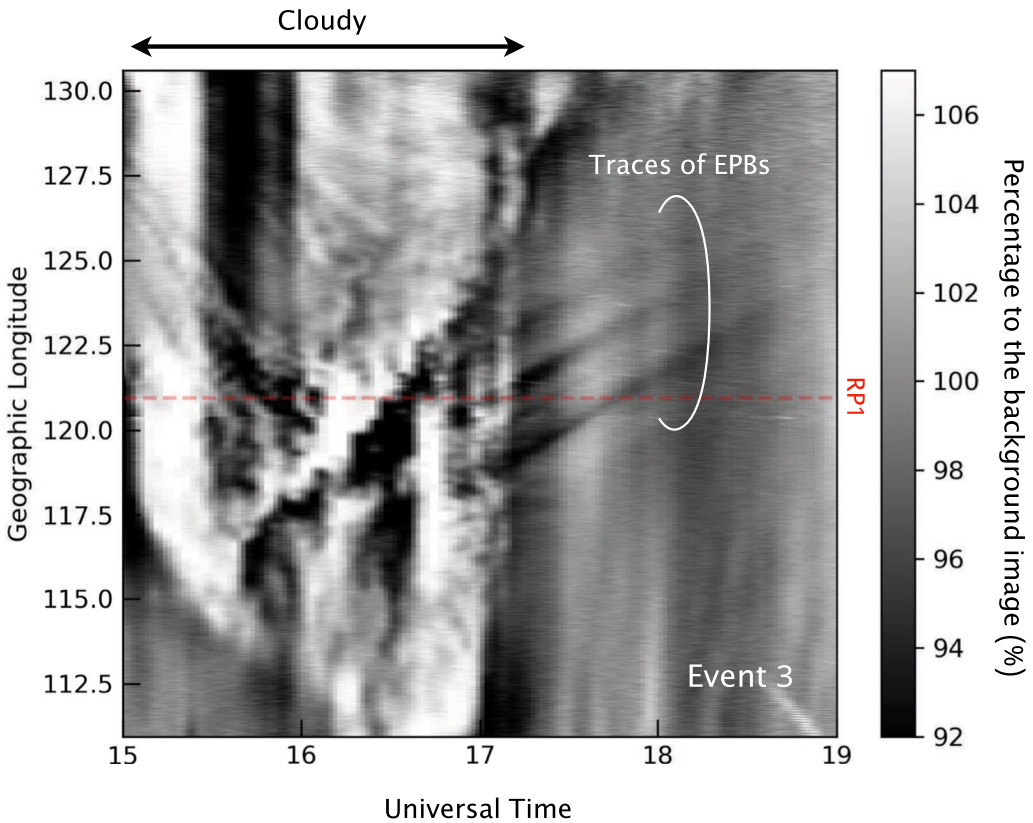


**Fig. 4** Airglow data during Event 3 plotted in a format of keogram, which was created by extracting the all-sky images at the geographic latitude of RP1. Although obscured by clouds between 15:00 and 17:00 UT, four traces of eastward moving EPBs are identified as black linear structures extending upward to the right from 17:00 to 18:30 UT

right. These oblique traces reflect the increase of longitude with time, indicating the eastward motion of the EPBs. Furthermore, since the slope of the traces in the keogram remained relatively constant over time, it is apparent that EPBs were drifting eastward at a constant velocity. By calculating the slope of the EPB traces in the keogram, the average east–west velocity of EPBs was determined to be 105 m/s for Event 1, 54 m/s for Event 2, and 85 m/s for Event 3. Chum et al. (2014, 2016) estimated the propagation velocity of OSS by using its frequency variation and time lag between the data from multiple stations. The estimated propagation velocities of OSS were mostly between 70 and 170 m/s. The estimates of the eastward drift velocities obtained from HFD sounder for Events 1, 2, and 3 are 120, 60, and 70 m/s with uncertainties of about ± 20 m/s, respectively, providing another evidence for the identity of OSS and EPB. Here, we estimated those velocity values following the method of Chum et al. (2014, 2016) using time lags between the data from multiple stations. It is worth noting that the change of the reflection altitude does not affect the calculation since we use the propagation delay between three reflection points (the geographical location of the reflection point can be derived without any assumptions of reflection height).

## Discussion

First, we discuss the relationship between the internal sub-structure of OSS and the branching structure of EPB. Figure 5a displays a representative airglow image from Event 3, at 17:13 UT on March 16, 2015. At this time, six branches of EPB are seen in the equatorward part of the image which are indicated by the yellow dashed lines. Figure 5b shows the Doppler spectrogram obtained during Event 3, including the time displayed in Fig. 5a. The fine-scale sub-structures of the OSS can be identified for all the three points. Specifically, at RP2, six structures can be identified as indicated by the red lines, corresponding to the number of branches of EPBs shown in Fig. 5a. This supports the idea that the sub-structures of OSS are manifestations of branching structures of EPB.

By close comparison between the OSS signatures at the three reflection points in Fig. 5b, it is found that the sub-structures are most pronounced in the data from RP2 though the latitudes of the three reflection points are not much different. The only difference between the

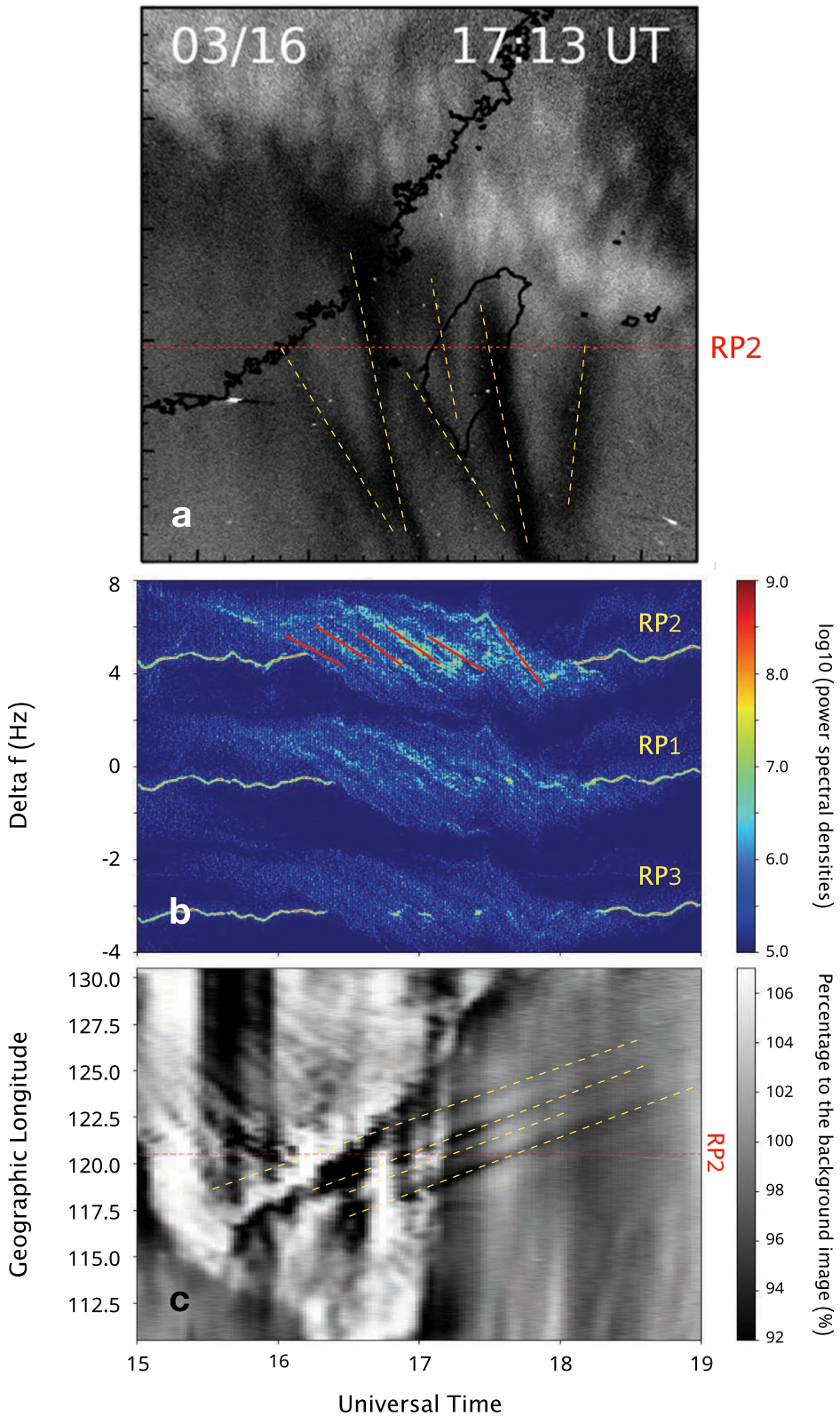


**Fig. 5** Detailed comparison between the sub-structures of OSS and the branches of EPB for Event 3. **a** A 630.0 nm airglow image at 17:13 UT on March 16, 2015, mapped onto the geographic coordinate system. **b** The Doppler spectrogram obtained between 15:00 and 19:00 UT on March 16, 2015. **c** The longitudinal keogram extracted at the latitude of RP2

three reflection points is the orientation of the ray path. Specifically, the ray path including RP2 is aligned more to the meridional direction, i.e., the typical direction of the elongation of EPBs. We speculate that, when the ray path is aligned more to the elongation of EPBs, the sub-structures of OSS (i.e., fine-scale features of EPBs) would become clearer.

Figure 5c again depicts the longitudinal keogram of the airglow images during the same time period, sampled at the exact latitude of RP2 (Glat 24.15N), which was indicated by the horizontal dotted line in Fig. 5a. Although it is cloudy during the first half of the period, the four traces of EPB were seen to move eastward at this latitude, which were outlined by the dashed yellow line. While six branching structures can be seen in the all-sky image of Fig. 5a, only four of them have reached the latitude of RP2. That is, the number of EPBs reached the reflection point RP2 is smaller than that of sub-structures of OSS seen at that sensing area. This suggests that, even if EPBs do not reach the estimated reflection point (i.e., intermediate point between Tx and Rx stations), the HFD sounding system can detect corresponding signatures in the Doppler spectrogram.

Next, we examine at which altitude the EPB-related ionospheric disturbances introduced radio wave reflection. By creating longitudinal keograms at a fixed latitude including reflection points of HFD, it is possible to estimate how the EPBs propagated in the longitudinal direction, i.e., the temporal variation of the longitude of EPBs. Assuming that reflection occurs at longitudes where EPBs exist, that is not necessarily at the midpoint reflection point, a time series of phase path length can be derived. This enables estimation of the Doppler shift from the temporal changes in phase path length using Eq. (1). The phase path length also depends on the altitude of reflection; thus, different Doppler shifts would be obtained for different assumption of the reflection altitude. Based on this relationship, an estimation of the reflection altitude was performed by adjusting the reproduced Doppler traces to the actual observed ones. More specifically, we have reproduced the Doppler shifts for various assumptions of reflection altitude and selected one that best explained the observed slope of the OSS traces.

The two panels of Fig. 6 again show the Doppler spectrogram from 15:00 to 19:00 UT on March 16, 2015

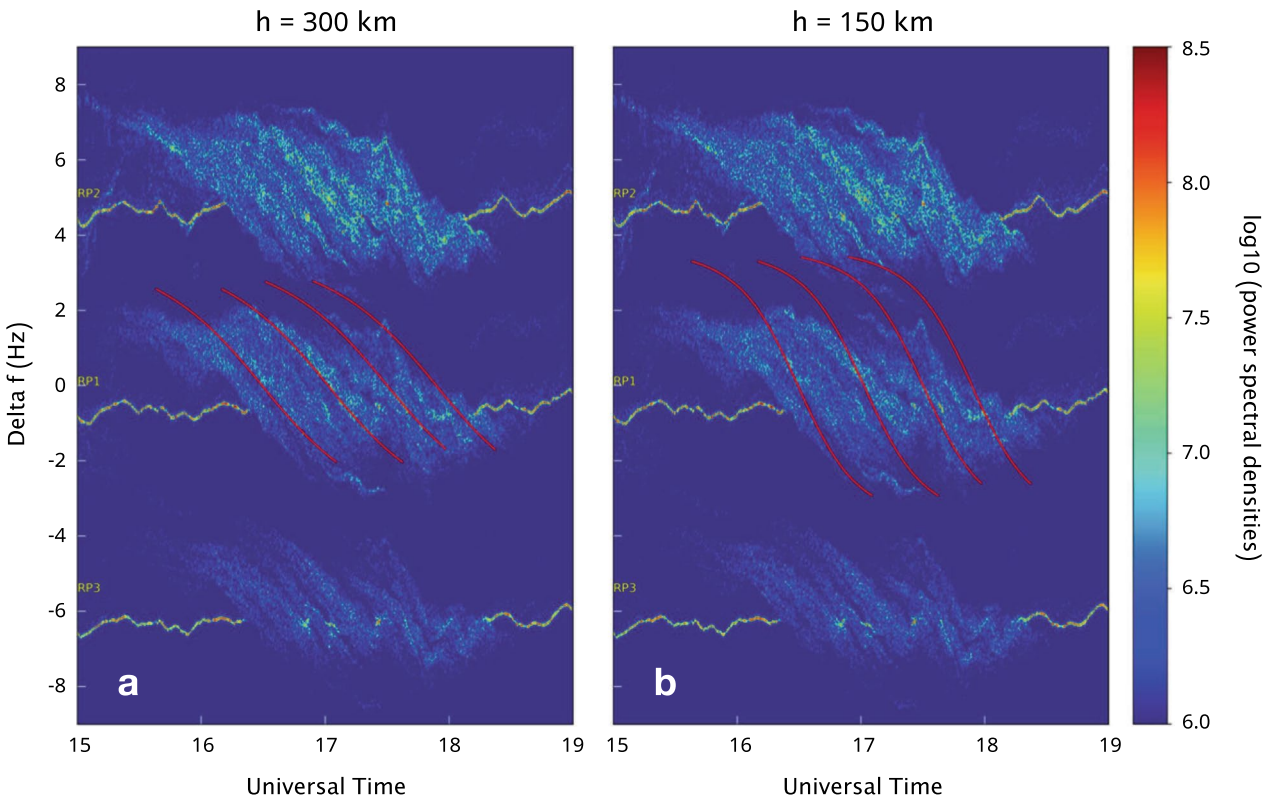


**Fig. 6** Estimation of reflection altitude through comparison between reproduced and observed OSS traces. **a** Doppler spectrogram of Event 3 where the Doppler shifts, estimated by assuming the reflection altitude at 300 km, are overplotted. **b** The same Doppler spectrogram as (**a**) but with the Doppler shifts estimated by assuming the reflection altitude of 150 km

(Event 3), where the reproduced Doppler shifts are superimposed with the red lines. Figure 6a assumes a reflection altitude of 300 km for calculating the Doppler shift, while Fig. 6b assumes 150 km. It can be seen that more consistent results are obtained when assuming the reflection altitude of 300 km, which agrees better with the observed slope of the OSS sub-structures. For Event 3, a best correspondence was obtained when assuming a reflection altitude of 300 km, as shown in Fig. 6. This value is slightly higher than the typical altitude of OI 630.0 nm airglow emission at around 250 km. This difference in the altitude of HFD reflection and airglow emission may be the reason for the difference in the visibility of the OSS/EPB signatures.

Similar analysis was conducted for Event 1, which was recognized as having a recognizable slope in the OSS trace. It was found that the most reasonable reproduction of the actual OSS slope was obtained when assuming a reflection altitude of 250 km. These altitudes are believed to correspond to the altitude at which ionospheric disturbances associated with EPBs exists. In other words, if the EPB-related disturbances existed (and moving eastward) at the F-region altitudes in the vicinity of the reflection point, those disturbances are observed as OSS in the HFD observation.

## Summary and conclusion

In this study, we performed a detailed analysis of the oblique spreading structure (OSS) often seen in Doppler spectrograms from HFD measurements, which was first introduced by Chum et al. (2016) as a possible signature of equatorial plasma bubble (EPB) in the radio observation. Three OSS cases were investigated based on simultaneous observations with a HFD sounding system and an all-sky airglow imager at low latitudes in Taiwan. The close correspondence between the appearance of optical signatures of EPBs at the HFD sensing area and the occurrence of OSS in the Doppler spectrograms well supports the expectation of Chum et al. (2016) that OSS are manifestations of EPBs in the HFD measurements. The eastward propagation speed of EPBs derived from the consecutive airglow images was also consistent with the speed of OSS estimated from the HFD data, which again confirms that the origin of OSS is ionospheric variation associated with EPB (or ESP). Furthermore, by comparing the branching structure of EPBs with the fine-scale traces within OSS, it was suggested that the sub-structure within OSS represents the branching structure of EPBs, demonstrating the possibility of inferring the spatial structure of EPBs from the morphology of OSS in HFD data.

### Abbreviations

| | |
|---|---|
| EPBs | Equatorial plasma bubbles |
| GNSS | Global navigation satellite system |
| OSS | Oblique spread structure |
| ESF | Equatorial spread F |
| UT | Universal time |
| HF | High frequency |
| HFD | High-frequency Doppler |
| VHF | Very high frequency |

### Acknowledgements

KH thanks J. Sakai for helpful discussion.

### Author contributions

HS carried out most of the data analysis and prepared the manuscript. KH carried out the data analysis and edited the manuscript. HN discussed the signature of EPB in the HFD data. JC processed the HFD data from Taiwan and discussed the results. CHL. and JTL processed the all-sky airglow imager data from Taiwan and discussed the results. All the authors reviewed the manuscript.

### Funding

This work was supported by the collaboration research project of Electric Navigation Research Institute (ENRI).

### Availability of data and materials

Data of HF Doppler observation in Taiwan employed in this paper are available upon request (contact: Jaroslav Chum). Data of the airglow imager in Tainan, Taiwan are also available upon request (contact: Chien-Hung Lin and Jia-Ting Lin).

## Declarations

### Ethics approval and consent to participate

Not applicable.

### Consent for publication

Not applicable.

### Competing interests

The authors declare that they have no competing interests.

### Author details

[1]University of Electro-Communications, Chofugaoka 1-5-1, Chofu, Tokyo 182-8585, Japan. [2]Graduate School of Engineering, Chiba University, Chiba, Japan. [3]Institute of Atmospheric Physics of the Czech Academy of Sciences, Bocni II/1401, 14101 Prague 4, Czech Republic. [4]Department of Earth Sciences, National Cheng Kung University, Tainan, Taiwan.

Received: 9 May 2023 Accepted: 21 September 2023
Published online: 10 October 2023

### References

Aarons J (1993) The longitudinal morphology of equatorial F-layer irregularities relevant to their occurrence Space Sci. Rev 63:1993

Berkner LV, Wells HW (1934) F-region ionosphere-investigations at low latitudes. Terr Magn Atmos Electr 39(3):215–230. https://doi.org/10.1029/TE039i003p00215

Chum J, Bonomi FAM, Fišer J, Cabrera MA, Ezquer RG, Burešová D, Laštovička J, Baše J, Hruška F, Molina MG, Ise JE, Cangemi JI, Šindelářová T (2014) Propagation of gravity waves and spread F in the low-latitude ionosphere over Tucumán, Argentina, by continuous Doppler sounding: first results. J Geophys Res Space Phys 119:6954–6965. https://doi.org/10.1002/2014JA020184

Chum J, Liu JY, Chen SP et al (2016) Spread F occurrence and drift under the crest of the equatorial ionization anomaly from continuous Doppler sounding and FORMOSAT-3/COSMIC scintillation data. Earth Planets Space 68:56. https://doi.org/10.1186/s40623-016-0433-1

Gentile LC, Burke WJ, Rich FJ (2006) A global climatology for equatorial plasma bubbles in the topside ionosphere. Ann Geophys 24:163–172. https://doi.org/10.5194/angeo-24-163-2006
Kil H (2015) The morphology of equatorial plasma bubbles—a review. J Astron Space Sci 32:13–19
Kil H, Paxton LJ, Oh S-J (2009) Global bubble distribution seen from ROCSAT-1 and its association with the pre-reversal enhancement. J Geophys Res 114:A06307. https://doi.org/10.1029/2008JA013672
Kintner PM, Ledvina BM, de Paula ER (2007) GPS and ionospheric scintillations. Space Weather 5:S09003. https://doi.org/10.1029/2006SW000260
Kubota M, Fukunishi H, Okano S (2001) Characteristics of medium- and large-scale TIDs over Japan derived from OI 630-nm nightglow observation. Earth Planets Space 53:741–751. https://doi.org/10.1186/BF03352402
Laštovička J, Chum J (2017) A review of results of the international ionospheric Doppler sounder network. Adv Space Res 60(8):1629–1643. https://doi.org/10.1016/j.asr.2017.01.032
Nakata H, Nagashima I, Sakata K, Otsuka Y, Akaike Y, Takano T, Shimakura S, Shiokawa K, Ogawa T (2005) Observations of equatorial plasma bubbles using broadcast VHF radio waves. Geophys Res Lett 32:L17110. https://doi.org/10.1029/2005GL023243
Otsuka Y, Shiokawa K, Ogawa T, Wilkinson P (2002) Geomagnetic conjugate observations of equatorial airglow depletions. Geophys Res Lett 29:43. https://doi.org/10.1029/2002GL015347
Otsuka Y, Shiokawa K (2006) Ogawa T (2006) Equatorial ionospheric scintillations and zonal irregularity drifts observed with closely-spaced GPS receivers in Indonesia. J Meteor Soc Jpn 84A:343–351
Rajesh PK, Lin CH, Chen CH, Chen WH, Lin JT, Chou MY, Chang MT, You CF (2017) Global equatorial plasma bubble growth rates using ionosphere data assimilation. J Geophys Res Space Physics 122:3777–3787. https://doi.org/10.1002/2017JA023968
Roettger J (1976) The macro-scale structure of equatorial spread-F irregularities. J Atmos Terr Phys 38:97–101
Sobral JHA, Takahashi H, Abdu MA, Muralikrishna P, Sahai Y, Zamlutti CJ, de Paula ER, Batista PP (1993) Determination of the quenching rate of the O(1D) by O(3P) from rocket-borne optical (630 nm) and electron density data. J Geophys Res 98(A5):7791–7798. https://doi.org/10.1029/92JA01839
Weber EJ, Buchau J, Eather RH, Mende SB (1978) North-south aligned equatorial airglow depletions. J Geophys Res 83:712–716
Woodman RF, LaHoz C (1976) Radar observations of F region equatorial irregularities. J Geophys Res 81:5447–5466

## Publisher's Note